AGU PUBLICATIONS

JGR

Journal of Geophysical Research: Space Physics

RESEARCH ARTICLE
10.1002/2015JA021447

Key Points:
- A new technique to detect topside EPB was applied to Swarm and TSX GPS data
- Morning EPB were seen over the Pacific Ocean during 6–8 h at storm recovery phase
- TIE-GCM shows enhanced vertical drifts near dawn due to disturbance dynamo

Supporting Information:
- Text S1
- Movie S1

Correspondence to:
I. Zakharenkova,
zakharen@ipgp.fr

Citation:
Zakharenkova, I., E. Astafyeva, and I. Cherniak (2015), Early morning irregularities detected with spaceborne GPS measurements in the topside ionosphere: A multisatellite case study, *J. Geophys. Res. Space Physics*, *120*, 8817–8834, doi:10.1002/2015JA021447.

Received 9 MAY 2015
Accepted 7 SEP 2015
Accepted article online 9 SEP 2015
Published online 7 OCT 2015

Early morning irregularities detected with spaceborne GPS measurements in the topside ionosphere: A multisatellite case study

Irina Zakharenkova[1], Elvira Astafyeva[1], and Iurii Cherniak[2]

[1]Institut de Physique du Globe de Paris, Paris Sorbonne Cité, Université Paris Diderot, UMR CNRS, Paris, France, [2]Space Radio Research Center, University of Warmia and Mazury, Olsztyn, Poland

Abstract We present observations of the equatorial plasma bubbles (EPB) in the topside ionosphere at early morning hours (05–08 LT) in the recovery phase of the 18–19 February 2014 geomagnetic storm. This rare type of irregularities was detected in the Pacific sector using GPS measurements on board several low-Earth-orbit (LEO) satellites. We use a multisatellite constellation consisted of the three Swarm and one TerraSAR-X satellites, that on 19 February flew in the same region and at similar altitudes ~500 km. The EPB occurrence in the LEO GPS data was observed for several consecutive orbits from ~11 UT to 16–17 UT on 19 February 2014, which suggests the following: (1) rather long duration (hours) of favorable conditions for EPB generation, (2) formation and evolution of EPB over wide longitude range of the Pacific Ocean, and (3) possible movement of the EPB region in the westward direction (with dawn). Registration of the early morning EPB in LEO GPS data was supported by concurrent in situ (Swarm and DMSP (Defense Meteorological Satellite Program)) and ground-based (ionosonde and GPS) measurements. LEO-based GPS technique is found to be essential and promising data source to study the topside EPB over regions with lack of the ground-based facilities. In addition, we use the Prompt Penetration Model and the Thermosphere-Ionosphere Electrodynamics Global Circulation Model (TIE-GCM) to identify the possible mechanisms responsible for the observed phenomenon. The model simulation results indicate the occurrence of the zone with the enhanced vertical plasma drift (~40–45 m/s) owing to the disturbance dynamo action in the predawn/dawn sector during 09–17 UT.

1. Introduction

Plasma density irregularities are observed in the equatorial ionosphere from the bottomside *F* region to altitudes of 1000–1500 km and are known as equatorial plasma bubbles (EPB) or equatorial spread *F*. This phenomenon has been extensively studied for many decades [e.g., *Farley et al.*, 1970; *Woodman and La Hoz*, 1976; *Ossakow and Chaturvedi*, 1978; *Fejer and Kelley*, 1980; *Ossakow*, 1981; *Tsunoda et al.*, 1982; *Jayachandran et al.*, 1993; *Hysell and Burcham*, 1998; *Kelley et al.*, 2011; *Hysell et al.*, 2013]. Out of a variety of measurement techniques used for the EPB detection-only satellites can provide observations on a global scale regardless of the ground-based facility positions. The detailed investigations on the EPB climatology, occurrence probability, and characteristics of EPB dynamics on a global scale are based on the in situ plasma probe measurements at various low-Earth-orbit (LEO) satellite missions like AE-E, DMSP, ROCSAT-1, CHAMP, and C/NOFS [e.g., *Basu et al.*, 1980; *Livingston et al.*, 1981; *Aggson et al.*, 1996; *Kil and Heelis*, 1998; *Huang et al.*, 2002; *Burke et al.*, 2004; *Rodrigues et al.*, 2009; *Xiong et al.*, 2010; *Huang et al.*, 2014]. These data represent a one-dimensional horizontal cut or a sampling when a satellite passes through the EPB structures.

Nowadays, space agencies launch more and more LEO satellites with different targets and instrument payloads; however, plasma density probe instrument is installed on board few satellites only. The question is—Can we derive more information about the ionosphere from satellites without a plasma density probe and other instruments for ionosphere research? Probably, yes. Recently, a new method for EPB detection was successfully implemented using the high-resolution magnetic field measurements on board the CHAMP satellite [*Stolle et al.*, 2006; *Lühr et al.*, 2014]. Based on this method, the new product "ionospheric bubble index" is generated for the European Space Agency (ESA) mission Swarm [*Park et al.*, 2013]. This method allows the detection of the EPB magnetic signatures along a LEO satellite orbit, and it is also one-dimensional measurement.

Here we introduce a new method for the onboard GPS measurements implementation for detection of the topside plasma irregularities. We demonstrate that the LEO GPS data, intended for the satellite positioning, have supplementary advantages for 2-D and 3-D upward scanning of the ionosphere by multiple radio rays between a LEO and the GPS satellites. Recently, *Zakharenkova and Astafyeva* [2015] showed the advantages of an "additional" use of the precise orbit determination (POD) GPS measurements on board a single LEO satellite (CHAMP) in multiinstrumental analysis of the ionospheric irregularities. Here we present the first results of the EPB detection in the POD GPS data on the base of a multisatellite LEO constellation that include the Swarm mission. As EPB are mainly after-sunset and nighttime phenomena, we demonstrate the implementation of this technique for a case study of rather unlikely event—the EPB occurrence at the morning local time hours at the recovery phase of the moderately intense geomagnetic storm of 19 February 2014.

2. Data and Method Used

2.1. LEO ROT/ROTI Method

Data of the POD antenna of a spaceborne GPS receiver can be used not only for the POD purposes but also to estimate the topside total electron content (TEC) between a LEO satellite and a GPS satellite. *Pi et al*. [1997] introduced into usage two GPS-based indices: ROT and ROTI. ROT (rate of TEC change) is the time derivative of TEC and is considered as a measure of the phase fluctuation activity. ROTI (rate of TEC index) represents a standard deviation of the ROT over a selected time interval. The ROTI characterizes the severity of the GPS phase fluctuations and detects the presence of the ionospheric irregularities, as well as it measures the irregular structure of the TEC spatial gradient. This method has already proved its effectiveness for the ground-based GPS data [e.g., *Aarons and Lin*, 1999; *Ma and Maruyama*, 2006; *Nishioka et al*., 2008; *Sripathi et al*., 2011; *Demyanov et al*., 2012; *Jakowski et al*., 2012; *Astafyeva et al*., 2014; *Cherniak et al*., 2014].

Here we propose to apply this ROT/ROTI technique to the topside LEO GPS measurements. The major specific difficulties relate to the fast movement of a GPS receiver along an orbit and rather short duration of a LEO-GPS tracking session (10–20 min versus 2–5 h for a fixed, ground-based GPS receiver). On the other hand, we get a better global coverage for ROT/ROTI data distribution. The main steps in the POD GPS data processing are the following. First, from the data of a GPS receiver on board a LEO satellite we calculate a relative slant TEC along a line of sight (LOS) LEO-GPS. Dual-frequency phase measurements at L_1 and L_2 carrier frequencies provide very accurate relative slant TEC values that can be defined by equation (1) [e.g., *Hofmann-Wellenhof*, 2001]:

$$\mathrm{sTEC} = \frac{f_1^2 \cdot f_2^2}{f_1^2 - f_2^2} \cdot \frac{L_1 - L_2}{K} \tag{1}$$

where $f_1 = 1575.42$ MHz and $f_2 = 1227.60$ MHz are the carrier frequencies of the GPS signals and $K = 40.3\ \mathrm{m^3\ s^{-2}}$. After the slant TEC calculation, we reprocess the data to detect and correct cycle slips and to remove outliers.

The ROT is determined by taking the ratio of the difference between the slant TEC values at two successive times to the time interval [*Pi et al*., 1997]:

$$\mathrm{ROT} = \frac{\mathrm{sTEC}_k^i - \mathrm{sTEC}_{k-1}^i}{t_k - t_{k-1}} \tag{2}$$

where i is a GPS satellite and t_k is an epoch time. The ROT values are calculated and then detrended for all LOS with elevation angle over 40°. The ROT is calculated for each visible GPS satellite over a LEO position in units of TECU/min, where $1\ \mathrm{TECU} = 10^{16}\ \mathrm{el/m^2}$. The ROTI represents the standard deviation of the ROT for 1 min interval (equation (3)):

$$\mathrm{ROTI} = \sqrt{\langle \mathrm{ROT}^2 \rangle - \langle \mathrm{ROT} \rangle^2} \tag{3}$$

The global distribution of the ROTI values are presented in the form of the ROTI maps that were made by projecting the ROTI values on the Earth from the ionospheric piercing point at a fixed altitude (here 550 km). Along a satellite pass, we use a grid of $1° \times 5°$ resolution in latitude and longitude, respectively. The value in every cell is calculated by averaging all ROTI values covered by this cell area. *Zakharenkova and Astafyeva* [2015] analyzed the ROTI values derived from the CHAMP GPS data. The present paper focuses on the detailed study of the ROT estimates along LEO satellite passes and on how we can take a new advantage of using the GPS ROT/ROTI data from a multisatellite constellation.

2.2. Multisatellite Database: Swarm, TerraSAR-X, and DMSP Missions

GPS measurements on board the Swarm constellation were processed and analyzed in this study. The Swarm mission was launched on 22 November 2013, and it consists of three satellites—Swarm Alpha (A), Bravo (B), and Charlie (C) (named hereafter SWA, SWB, and SWC, respectively)—two of them are supposed to fly in a tandem separated by 1°–1.4° in longitude at an orbit altitude of 460 km, while the third satellite—at an orbit altitude of 510 km. The orbit commissioning was finalized by April 2014. However, during the event under consideration (19 February 2014), the Swarm constellation configuration was rather specific: all three satellites had an orbit altitude of ~490–500 km. The commissioning phase for the final orbit configuration was just started on February 2014, and several orbit maneuvers took place during this month. As a result, the orbit configuration was modified from the previous one like "pearls on a string" with several minute separations between the Swarm satellites that took place at the very early stage of the mission. As of 19 February 2014, the configuration was the following: a tandem of two satellites SWB&SWC followed SWA by ~30 min.

The nominal orbit inclination is 87.5°. Each satellite has a eight-channel dual-frequency GPS receiver on board. Before July 2014 the Swarm GPS data were released with the 10 s sampling rate; after July 2014 the raw GPS data are available with the 1 s sampling rate. All Swarm satellites are also equipped with a Langmuir Probe (LP) instrument to measure the in situ electron density (N_e). Swarm LP plasma density was released on 5 February 2015 within the Swarm preliminary plasma data set, and these data are not yet calibrated to the absolute values. According to the first quick comparison with other independent measurements and models, the current values are up to a few 10% too high at low density [*Preliminary L1b Plasma Dataset*, 2015].

Besides, the Swarm observations, here we use GPS measurements on board the TerraSAR-X satellite. TerraSAR-X, named hereafter TSX, is a German synthetic aperture radar (SAR) Earth observation satellite launched in June 2007. It had a Sun-synchronous dawn-dusk orbit with an inclination of 97.5°. The orbit altitude was about 515 km—very similar to the Swarm constellation. TSX is equipped by a 12-channel dual-frequency GPS receiver and delivers data with 10 s resolution.

In addition to the Swarm and TSX GPS data, we analyze the in situ ion density Ni measured at ~840 km by the DMSP (Defense Meteorological Satellite Program) F16, F17, and F18 satellites, as well as data from ground-based GPS receivers and digisondes.

3. Geomagnetic Disturbances of 18–20 February 2014

Two geomagnetic storms of 18–20 February 2014 were provoked by a series of Earth-directed coronal mass ejections (CME). The IMF B_z component turned negative at ~13:20 UT on 18 February 2014 and resulted in a negative excursion of *SYM-H* (Figure 1). When the second CME reached the Earth's magnetopause at ~04 UT on 19 February, the IMF B_z component further intensified to −15 nT. The IMF B_z remained negative until ~09 UT, and the *SYM-H* index decreased to the minimum value of −125 nT at ~08:20 UT on 19 February 2014. The subsequent northward turning of the IMF marked the beginning of the recovery phase with a reduction of the *SYM-H* to −40 nT in ~8 h. The planetary *K* index (*Kp*) reached the maximum of 6 during 06–09 UT on 19 February (Figure 1c). This storm was accompanied by high substorm and magnetic activities in high-latitude regions, as seen from variations of the auroral electrojet (*AE*) (Figure 1b).

Here we focus on the time period from 10 to 18 UT on 19 February 2014, which correspond to the recovery phase of the storm, and when the intensive ionospheric irregularities occurred.

4. Results and Discussion

4.1. Satellite Observations of the Topside Ionospheric Irregularities at Early Morning Hours of 19 February 2014

As mentioned before, during the 19 February 2014 event the Swarm and TSX satellites had a very similar altitude of ~500 km, and the TSX and SWA passed the same region but in the opposite direction. We apply the LEO ROT/ROTI technique to the Swarm and TSX GPS measurements to examine the occurrence of the topside ionospheric irregularities in the predawn sector. Figure 2 presents the global maps of the ROTI variability along the Swarm and TSX satellite passes during the day of 19 February 2014 (Figures 2b, 2c, 2d, and 2f) and the average ROTI maps for the morning sector (Figures 2a and 2e). In the morning sector, all Swarm satellites fly from south to north direction and TSX from north to south. To obtain a reference map

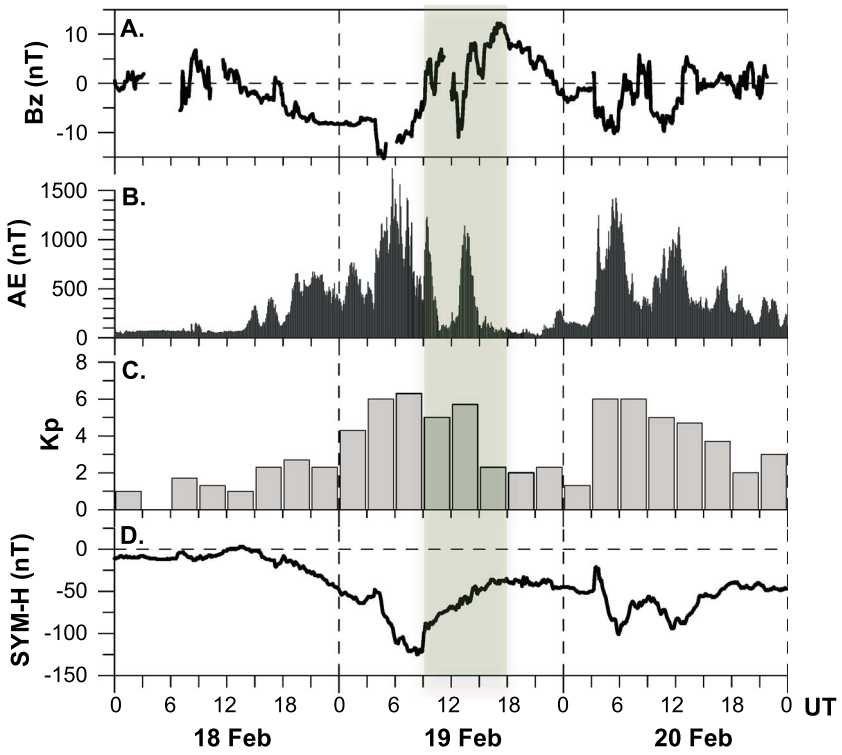

Figure 1. Variations of the interplanetary and geomagnetic parameters during 18–20 February 2014 storm: (a) IMF B_z component (not time shifted), (b) auroral electrojet index *AE*, (c) planetary index *Kp*, and (d) index of geomagnetic activity *SYM-H*. The shaded area indicates the period of intense EPB observation.

under quiet conditions we calculate the average ROTI map. Swarm ROTI map (Figure 2a) corresponding to 6.5–7.5 LT was calculated from the set of Swarm data for seven previous quiet days with the daily *Kp* sum less than 20. Due to the fast shift of the Swarm orbit plane to another LT sector, we could not use many days for data averaging. The situation was different for the Sun-synchronous TSX orbit and the TSX ROTI map (Figure 2e), which was averaged over 30 quiet days and corresponded to 5.5–6.5 LT. Taking into account the time difference between these maps, we can conclude that generally in February 2014 in the morning sector the topside GPS fluctuations over low latitudes were very small (ROTI $<$ 1.0–1.5 TECU/min). This quiet picture changed significantly on 19 February 2014, when three Swarm satellites independently registered the occurrence of strong GPS fluctuations with significantly increased ROTI values along several successive passes over the Pacific Ocean. The most intensive irregularities that corresponded to very high ROTI values (5 TECU/min and higher) were detected by the SWA satellite (Figure 2b). The irregularities were found to occur starting from ~12 UT, lasted until 17–18 UT and covered the Pacific Ocean within longitudes of 170°W–80°W. SWB&SWC and TSX registered intense irregularities close to longitudes 100°W–90°W during 12.0–13.5 UT. As the Swarm and TSX altitude was ~500 km, the GPS phase fluctuations were detected above this altitude and they were related to plasma irregularities in the topside ionosphere, even though these irregularities are elongated structures from the bottomside ionosphere or they are the separated structures drifted above the 500 km altitude.

Therefore, the LEO ROTI index can be effectively used to detect the presence of the topside ionospheric irregularities and even indicate the intensity of these irregularities. More detailed information can be obtained from the analysis of the LEO ROT values that show the TEC changes along a LOS from a LEO to selected GPS satellites. However, for the LEO ROT data we could not use the standard form of the ROT representation. For the ground-based GPS observations we usually use the graph with all satellites visible over a GPS station during 24 h (e.g., Figures 4b and 4c). For the LEO ROT data, the GPS receiver does not have a fixed position since it is on board a satellite, and the time duration of a LEO-GPS tracking session is rather short (10–20 min) in comparison with a ground-based one (2–5 h). Below we propose a possible way of the LEO ROT data representation suitable for comparison with other observations.

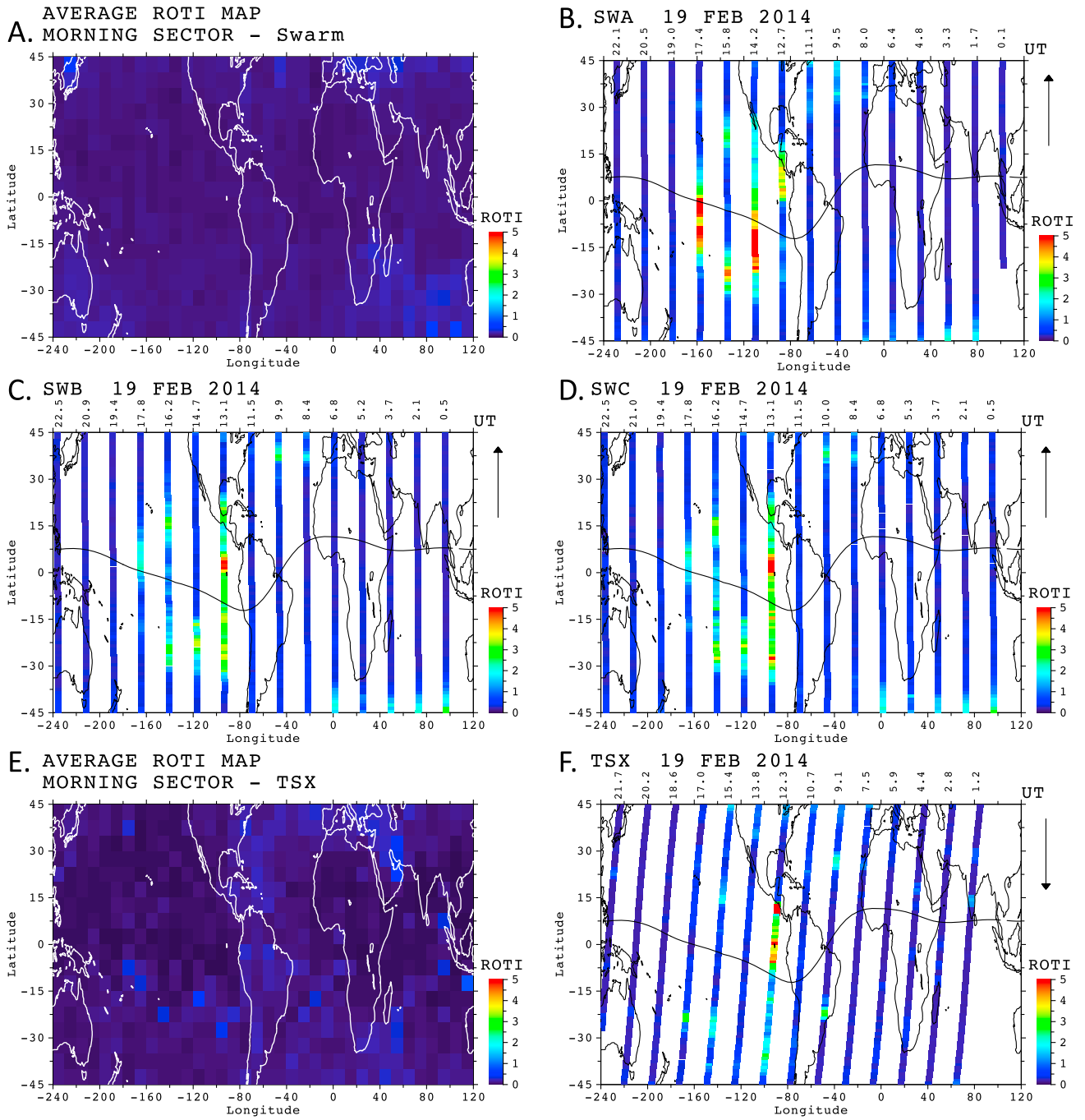

Figure 2. Global maps of the ROTI variability for the morning sector: the average ROTI map for quiet conditions from (a) Swarm and (e) TSX data; ROTI variability along passes for (b–d) three Swarm satellites and (f) TSX on 19 February 2014. All passes are shown in chronological order from right to left. Approximate equator crossing time in UT is indicated at the top part of each graph, the equator crossing time was about 6.7 LT and 6.0 LT for TSX.

Figure 3 presents in detail the dawn-time registration of the topside irregularities along three successive orbital tracks. Due to the favorable orbital configuration of the Swarm satellites and TSX these observations were separated into the following time series: the first pair of TSX and SWA, the next one—the tandem of SWB&SWC, appeared in the same region but ~30 min later. The GPS satellites were selected in such a way to make observations by all LEO satellites with rather high elevation angles and long duration. Each left plot of Figure 3 demonstrates the sketch view in geographical coordinates for the DMSP and Swarm satellite tracks, subionospheric tracks for LOS from LEO to GPS, and the right plots demonstrate changes of the

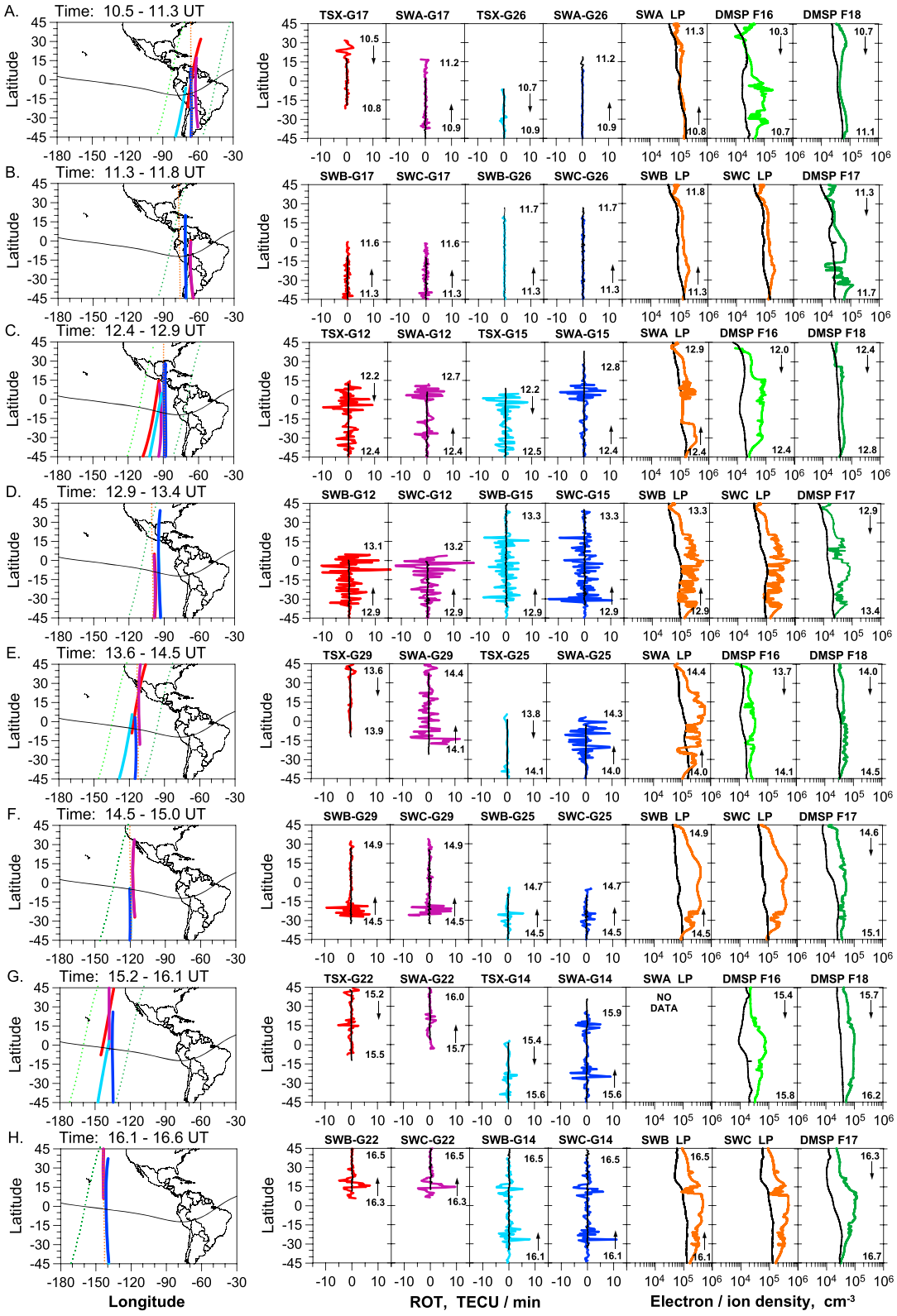

Figure 3. (a–h) Registration of the topside ionospheric irregularities for different instants of time. Each panel illustrates: (left) geographical map with subionospheric track coordinates at 550 km altitude for LOS from Swarm A, B, C and TSX to specific GPS satellites and (right) ROT for corresponding satellites (red, magenta, cyan, and blue curves) and in situ Swarm electron density (orange curve) and DMSP ion density (green curves); black lines present the reference values for previous quiet day. Mark like "SWA-G17" means the data along LOS between LEO SWA and GPS PRN 17. Graphs contain information about starting-ending time and direction of the measurements marked by arrows. Minutes are indicated in the decimal format.

ROT and in situ density along the corresponding tracks given as functions of a geographical latitude. Although Swarm LP data are not yet calibrated to the absolute values, these data are very useful to examine the relative variability of the plasma density along a satellite's orbit. The GPS satellites are indicated with a pseudo random noise (PRN) satellite number.

Figure 3a shows the satellite measurements during 10.5–11.3 UT: two satellites—SWA and TSX—cross the region of the South America from the opposite directions and are able to track GPS PRN 17 and 26; besides, we have the in situ LP density for the SWA and the ion density from two DMSP satellites that passed on the east and west sides. ROT data show the presence of rather weak (e.g., SWA-G26) or moderate phase fluctuation activity; the most intense phase perturbations were registered within latitude range of 15°–30° N along LOS TSX-G17 at 10.6–10.7 UT. The Swarm LP density profiles also detect small irregularity structures above 490 km over 15°N–45°N latitude range. Latitudinal plasma (ions) density profile measured by DMSP F18, crossed the region from the east, detects no or very weak density irregularities at altitude of 840 km during 10.7–11.1 UT. However, DMSP F16, that passed within 15°–20° on the west from this region, detected significant plasma irregularities during 10.3–10.7 UT, that is the evidence that the irregularities appeared in the bottomside ionosphere in this sector of the Pacific Ocean before 10.7 UT and already propagated upward to altitudes of 840 km. These irregularities correspond to 4.7–4.9 LT.

Figure 3b illustrates the development of the situation during 11.3–11.8 UT, when the tandem SWB&SWC, flying over the same region off the west coast of the South America, simultaneously tracks GPS PRN 17 and 26; in addition, the in situ LP density from both SWB&SWC satellites and one DMSP pass on the west were available. Looking on the ROT data, we can note similarities in the results derived independently from the SWB&SWC satellites. Both tracks LOS PRN 17 and 26 are located on the east from the Swarm pass and demonstrate rather weak irregularities. DMSP F17 passed the same way as F16 1 h before and also registered the presence of the strong plasma density fluctuations with clear depletions at 840 km within 15°–45°S latitudes. The DMSP-detected irregularities corresponded to 5.5 LT. Simultaneous observations indicate that during 10.5–11.8 UT both GPS and LP data did not detect strong plasma irregularities above 480–500 km in South America region (60°W–80°W, 15°N–45°S), but at the same UT interval plasma irregularities above 840 km were measured by DMSP satellites near 90°W longitude, that was in 1–1.5 h LT distance from the Swarm satellites.

The first entrance of the TSX and SWA satellites to the region, where DMSP had already registered irregularities, was after ~12 UT (Figure 3c). The TSX came from the north and detected intense ROT fluctuations on both LOS G12 and G15. The most intense irregularities in TSX data were found to occur at 5.8–6.0 LT. Then these two GPS satellites were tracked by SWA and recorded the irregularities occurrence at the same latitudes and with similar intensity. GPS phase fluctuation activity was about 5–10 TECU/min, and the zone with maximal intensity was within 15°N–15°S latitude range. The track of LOS SWA-G15 was practically co-located with SWA pass, and we note the coincidence of the intense plasma irregularities zone around 0°N–15°N in both GPS ROT and LP observations. These irregularities were detected at 6.6–6.7 LT. DMSP F16, flew on the west from this zone, demonstrates the significant enhancement of the plasma density at 840 km around 15°N–30°S latitudes with smaller-scale structures inside. On the east, over the coast of South America, DMSP F18 did not detect EPB at ~840 km.

The SWB&SWC tandem appeared over this region ~30 min after the SWA and TSX (Figure 3d) and detected highly intense ROT fluctuations within the region of 90°W–100°W longitude and 40°S–15°N latitude. The intense GPS fluctuations reached up to 5–12 TECU/min comparing with 0.0–0.5 TECU/min during quiet time conditions of the previous day. These irregularities were recorded at 12.9–13.2 UT and corresponded to 6.6–6.8 LT. Swarm LP observations also revealed severe plasma density irregularities with the electron density enhancement over the same latitudinal region. Swarm data, both ROT and LP, confirm that EPB structures propagated to altitudes 480–500 km and above. DMSP F17 observed an increased EPB activity in comparison with F16 1 h before, but within 100°W–120°W longitudinal range. We emphasize that observations for the quiet day (black lines) do not record any EPB presence.

Figures 3e and 3f present the next satellite observations within the active region. The ROT data measured by the TSX satellite during 13.6–14.1 UT do not manifest any significant fluctuations, whereas after ~14 UT SWA recorded ROT fluctuation of 5–10 TECU/min along both LOS G25 and G29. We can note that the GPS LOS for Swarm and TSX differed in space; these ones for Swarm were very close to the SWA location along 115°W. Besides, the Swarm LP data at ~500 km altitude demonstrate intense plasma density irregularities with an

amplitude range similar to those observed by the tandem SWB&SWC along 100°W longitude 1 h before. Latitudinal plasma profiles measured by DMSP F16 and F18 above 840 km reveal relatively more intense irregularities on the west F16 track and rather small-scale irregularities at the east F18 track. The DMSP data indicate that the EPB activity over the considered region of 90°W–100°W becomes less intense after 14 UT in comparison to the previous hours. Figure 3f shows the occurrence of the ionospheric plasma irregularities above 500 km, which were detected in both Swarm GPS and LP measurements around 110°W–120°W longitude and limited by 15°S–40°S latitude range. Figures 3g and 3h show the registration of the EPB at the consequent orbital passes during 15.2–16.6 UT.

Analysis of the data from Figures 2 and 3 suggests that the zone with the EPB occurrence drifted westward with simultaneous decrease of intensity. We can clearly define the region within 90°W–100°W of longitudes, where all seven satellites—Swarm, TSX, and DMSP—recorded the maximal intensity of the ionospheric irregularities at altitudes above 500 and 840 km during 10.5–13.5 UT.

4.2. Ground-Based Observations

Our results demonstrate the occurrence of the EPB in the morning time (05–08 LT) over the Pacific Ocean region with the longitude range of 170°W–80°W. The maximal intensity of the topside irregularities was found at 90° W–100°W during 10.5–13.5 UT (05–08 LT). We use seven different satellites, but we are limited by this LT sector and the EPB can occur before and/or after the time when a satellite crossed this region.

To demonstrate that the most favorable conditions for the storm-induced morning time EPB occur only in this region of the Pacific Ocean, we further analyze the ground-based data. We select three equatorial ionospheric sounding stations: Jicamarca, Peru (geographic 11.9°S, 76.8°W, geomagnetic latitude 1.0°N), São Luis, Brazil (geographic 2.6°S, 44.8°W, geomagnetic latitude 2.4°S), and Guam, Mariana Islands (geographic 13.6°N, 144.8°E, geomagnetic latitude 5.6°N). The co-located GPS stations are JICA, SALU, and GUUG, respectively. We manually process the ionograms from the Global Ionospheric Radio Observatory DIDbase to retrieve the critical frequency (f_oF_2) and height (h_mF_2) of the F_2 layer peak [*Reinisch and Galkin*, 2011]. The F_2 peak density (N_mF_2) was calculated from f_oF_2 measurements. GPS measurements from the co-located ground-based GPS stations were processed to retrieve the ROT variability. Figure 4 shows (a) the N_mF_2 and h_mF_2 variations over these ionosondes and (b) ROT variations during 18 and 19 February 2014. The gray shaded area indicates the local nighttime. The intense irregularities at the JICA and SALU stations occur after the sunset during 20–01 LT for both quiet and disturbed days, whereas no GPS fluctuation activity can be seen at the GUUG station. On the storm day of 19 February, the ionosonde measurements over Jicamarca show a significant enhancement of the F_2 peak density during nighttime (02–07 LT). The h_mF_2 data demonstrate also the uplift of the F_2 layer for more than 100 km at the predawn time. Comparison with São Luis and Guam ionosondes reveals that such an uplift accompanied by the F_2 peak density enhancement was observed only at the Jicamarca ionosonde. This nighttime uplift of the ionospheric F_2 layer with peak density enhancement can be associated with the eastward electric fields. As a result, the favorable conditions occur for the EPB generation, and consequently, the equatorial spread *F* was observed at Jicamarca much longer until ~12:30 UT (07:30 LT) during the disturbance time (red/blue dashed line at Figure 4a). The predawn and morning time irregularities were also observed at the co-located GPS station JICA (Figure 4b, left).

Additionally, we find only three available GPS stations in the Pacific Ocean close to the region where the satellites detected the EPB occurrence: GLPS, ISPA, and CKIS. Figure 4c demonstrates the ROT variations over these ground-based stations. It is interesting to note that on the previous day of 18 February the GPS fluctuation activity was not observed over these three stations even during the after-sunset time. On the storm day of 19 February, we found strongly intense fluctuations over the GLPS station during the local evening time (20–00 LT). The second series of the GPS fluctuation intensification occur several hours before the sunrise and continued through the morning time (04–09 LT). For the ISPA station the severe GPS fluctuations were found only at the predawn-morning time (04–08 LT) and they were much more intense than that at other considered GPS receivers. At the CKIS station located at Cook Islands we found less intense GPS fluctuations occurred in the evening time (20–01 LT) and in the morning time (05–08 LT). We can note a similarity in the onset of the irregularities occurrence during nighttime, ~2 h before sunrise. On the other hand, we observe the westward displacement of the irregularities zone toward the center of the Pacific Ocean and rather large temporal extent of the irregularities detection at different stations from ~11 UT at the JICA station to ~18 UT at the CKIS station.

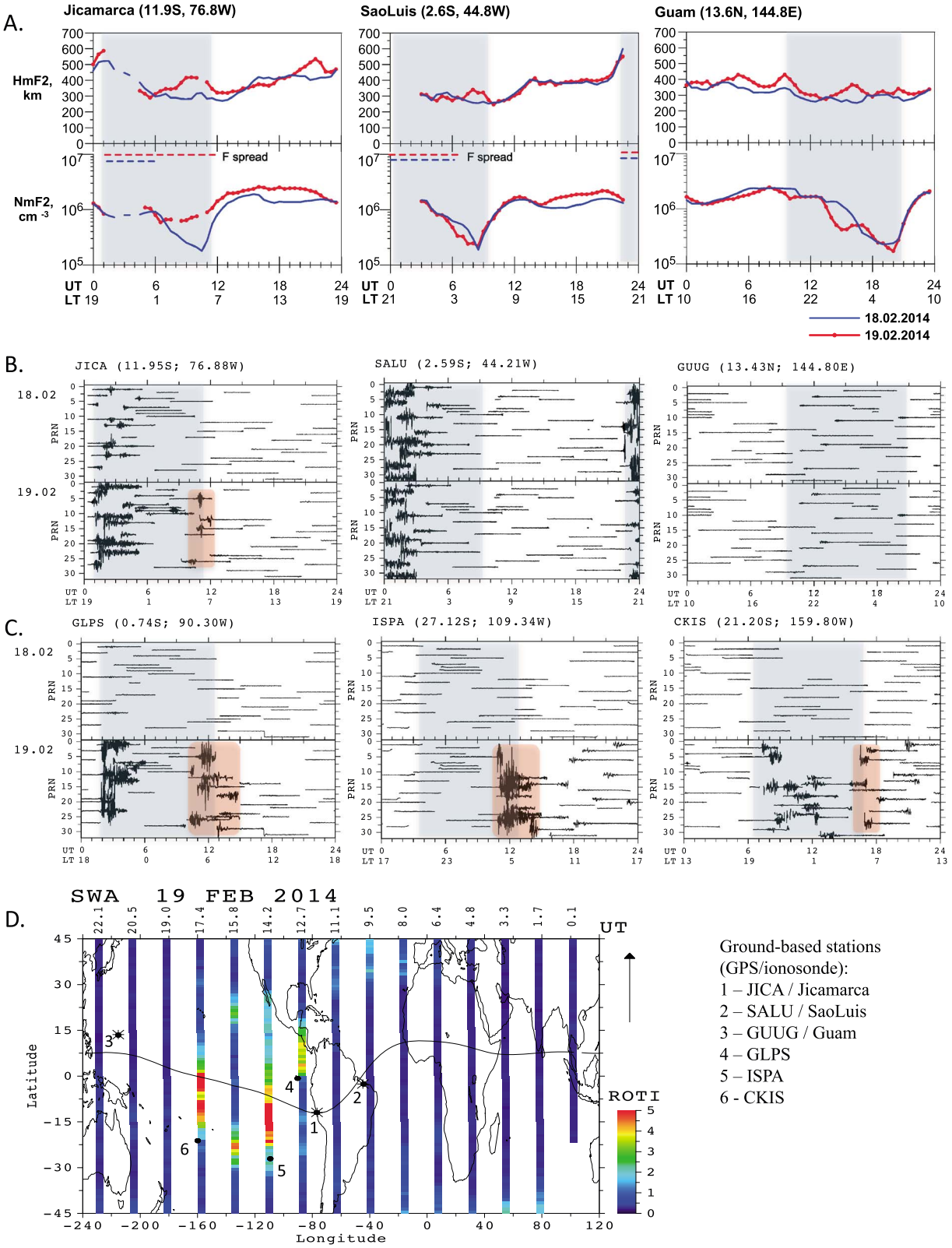

Figure 4. Ground-based measurements for 18–19 February 2014: (a) ionosonde-derived density (N_mF_2) and height (h_mF_2) of the F_2 layer peak over Jicamarca, São Luis, and Guam digisonde stations; (b) GPS ROT variations for the co-located GPS stations; (c) GPS ROT for three GPS stations in the Pacific Ocean; (d) geographical map with the positions of the SWA traces and ground-based stations. The ionosondes are marked by asterisks, GPS stations: by black dots. The grey shaded area shows the local nighttime period from the dawn-dusk terminator calculated at 100 km altitude. The dashed lines in Figure 4a show the duration of the equatorial spread *F*.

Figure 4d presents the overall view on the LEO ROTI intensity along the SWA satellite passes and locations of the ground-based stations. The GPS-based results from Figures 4b–4d can be summarized as follows: (1) ground-based GPS stations have a very sparse distribution in this region of the Pacific Ocean; (2) the most intense irregularities in the ground-based GPS data were observed at GLPS and ISPA stations, located on the west from the coast of South America; (3) GPS irregularities in the morning time were registered over four stations in the Pacific Ocean; and (4) there is a good agreement in time between the LEO ROTI data along the SWA passes and the ROT fluctuations in the morning time at the GLPS, ISPA, and CKIS stations. However, the ground-based GPS stations could not provide any information for the region where satellites have detected the occurrence of the most intense EPB. In this case, satellite measurements, in particular LEO GPS measurements, can be much more informative to study the EPB occurrence.

4.3. Possible Mechanisms: Model Simulations

The common mechanism explaining the generation of the EPB is the growth of the Rayleigh-Taylor instability, which, in turn, is initiated by the zonal electric field responsible for the upward vertical drift [*Farley et al*., 1970]. This vertical drift lifts of the ionospheric *F* layer to higher altitudes, which leads to the plasma instability and, consequently, to the occurrence of irregularities and scintillations [*Ossakow*, 1981; *Jayachandran et al*., 1993]. In general, the EPB have been regarded as the typical postsunset phenomena. Postmidnight and dawn EPB seem to stand out in a special rare "category." The EPB can occur in the local morning sector during a geomagnetic storm [*Fejer et al*., 1999] or, more rarely, independently on geomagnetic activity [*Burke et al*., 1979; *de la Beaujardière et al*., 2009]. Storm time conditions may promote or suppress the occurrence of EPB [*Fejer*, 1991]. *Basu et al*. [2001] found that storm-induced eastward electric fields can be associated with the strong EPB development and increase of the GPS TEC fluctuations and scintillations. *Yeh et al*. [2001] reported about presunrise EPB occurrence (03:00–04:30 LT) at the early recovery phase of the 22 October 1999 geomagnetic storm and found that these EPB were positively correlated with storm time eastward electric fields. During geomagnetic disturbances, the eastward electric field can arise from (1) prompt penetration of magnetospheric electric field and (2) electric field due to ionospheric disturbance dynamo [e.g., *Blanc and Richmond*, 1980; *Fejer*, 1997]. The disturbance dynamo electric fields are westward during the day and eastward at night. Therefore, if the storm-induced eastward electric fields occur at night, they can cause the F_2 layer uplift and promote the EPB generation.

For better understanding of the processes that control the EPB onset, the vertical plasma drifts ($E \times B$) should be analyzed. However, due to specific location of the zone with the detected morning time EPB (over the Pacific Ocean) we are rather limited in the availability of the reliable drift data, both ground-based and space-borne. The Jicamarca radar did not operate in the JULIA mode on 18–19 February 2014. The C/NOFS CINDI data were also unavailable for the day of 19 February 2014 due to a transmission failure (R. Heelis, private communication). We could not include into our analysis the Swarm-derived ion drift data, as the Swarm Thermal Ion Imager (TII) measurements on 18 and 19 February 2014 were seriously affected to varying degrees by the TII imaging anomaly (J. Burchill and D. Knudsen, private communication). Therefore, we involve into analysis the model simulation results in order to specify the possible physical mechanism of the dawn EPB generation over the Pacific region for the case of 19 February 2014.

4.3.1. Prompt Penetration Equatorial Electric Field Model

Ground-based GPS measurements over Jicamarca revealed that the morning time irregularities in GPS data occur during 10–12 UT on 19 February 2014 (Figure 4b). Further, we analyze the vertical plasma drift (V_z) of the ionospheric *F* layer derived from the Jicamarca digisonde measurements (Figure 5a). The Digisonde Portable Sounders operate essentially as radar systems; i.e., they measure radar distances and angles of arrival of the received echoes [*Reinisch*, 1996]. These digisondes use four small spaced antennas for signal reception arranged in a triangle with one antenna at the center. The signals from each antenna are Fourier analyzed to identify echoes with different Doppler frequencies. The drift velocity components are calculated from the line of site velocities (Doppler frequency shifts) of the skymap source points [*Reinisch et al*., 1998]. The *F* layer vertical drift measurements over the Jicamarca digisonde shows that the V_z suddenly increased from negative values (downward drift) to 36 m/s at 10:18 UT on 19 February 2014. This increase was of a short duration, the presented V_z values were nonsmoothed and indicated low error bars. During this V_z increase we observe also the F_2 layer uplift and the F_2 peak density enhancement (Figure 4a).

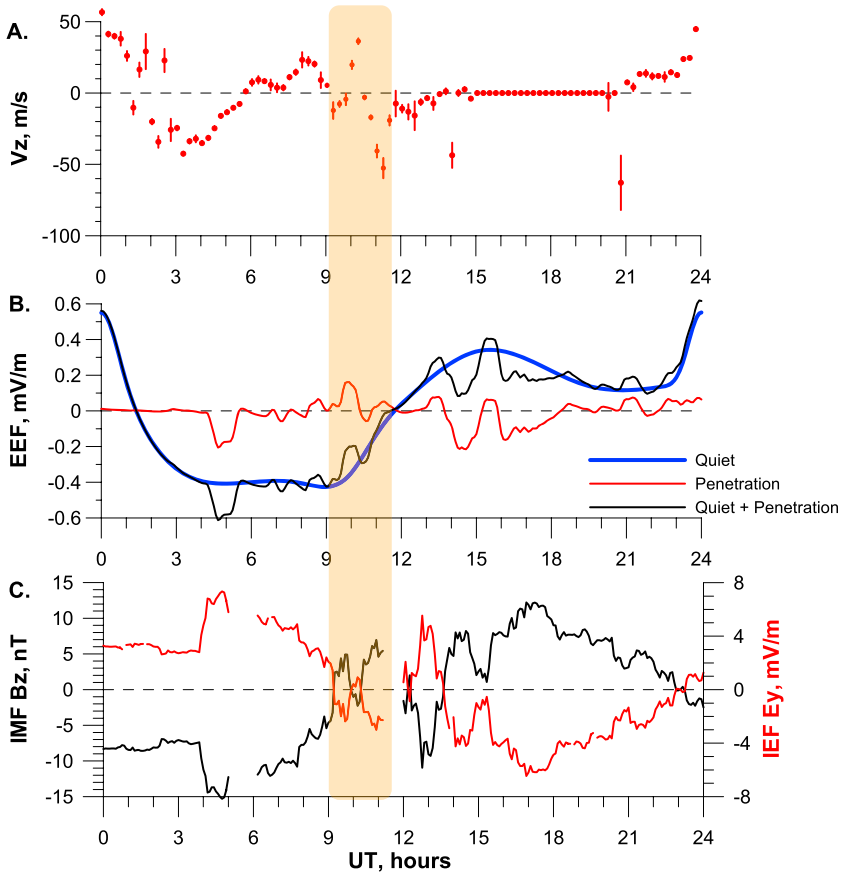

Figure 5. (a) *F* region vertical drift (nonsmoothed values) over Jicamarca digisonde (12.0°S, 76.8°W) during 19 February 2014. Error bars are shown by red thin lines. (b) Model calculation of the equatorial ionospheric eastward electric field (EEF) at longitude 77W for 19 February 2014. (c) IMF B_z component and estimated IEF E_y component (not time shifted).

Figure 5b presents the model calculation of the equatorial ionospheric eastward electric field (EEF) at the Jicamarca station longitude (77°W) for the conditions of 19 February 2014. We use the prompt penetration model [*Manoj and Maus*, 2012] that consists of a climatological model to account for the quiet day variations of EEF and a transfer function model to predict the prompt penetration contribution to EEF variation. To provide the climatological component of the zonal electric field (blue line in Figure 5b) *Manoj and Maus* [2012] use the quiet time *F* region equatorial vertical drift model by *Scherliess and Fejer* [1999]. The prompt-penetration model is driven by interplanetary electric field (IEF) data from the Advanced Composition Explorer (ACE) satellite.

We also plot in Figure 5c the IMF B_z and IEF E_y components changes occurred on 19 February 2014. At the OMNI website the IEF E_y component is estimated from the IMF measurements with assumption that the solar wind is due to the $E \times B$ drift of the interplanetary magnetic and electric field. Thus, the IEF E_y component is calculated as $E_y = -V_x \cdot B_z$, where V_x is the solar wind velocity and B_z is the IMF B_z.

As seen from Figure 1d, the storm recovery phase started at ~09 UT on 19 February 2014; however, at ~09:30 UT the IMF B_z abruptly turned southward from a steady northward direction and lasted ~40–45 min (Figure 5c). Correspondingly, the IEF E_y changed its direction during this period of time. The IEF E_y enhancement near 10 UT is seen in Figure 5c and in the model-derived estimation of the prompt penetration electric field at the Jicamarca longitude (Figure 5b, red line), as this model is driven by the same ACE IEF data. A positive step in the IEF with amplitude of 1 mV/m produces a zonal electric field response with the maximum amplitude of ~0.05 mV/m [*Manoj and Maus*, 2012]. Here the model predicts the appearance of the eastward directed prompt penetration field with the amplitude of ~0.2 mV/m. This peak and subsequent decrease of the predicted zonal electric fields are in close agreement with observations from the digisonde-derived vertical plasma

drifts (Figure 5a) with similar behavior pattern. Therefore, we can suppose that the occurrence of the ionospheric irregularities over the Jicamarca station during 10–12 UT on 19 February can be associated with the prompt penetration electric fields effects.

However, the GPS-detected irregularities were observed during rather long time interval (10–18 UT), and they were much more intense in longitude range of 90°W–120°W comparing to the ones at the Jicamarca longitude (Figure 4). Therefore, it is difficult to explain the dawn EPB occurrence over the Pacific Ocean by the action of the prompt penetration fields only.

The second principal source of a variation in the ionospheric electric field is the neutral wind disturbance dynamo effect. Comparing with the short duration of the prompt penetration fields, the disturbance dynamo effect is characterized by time scales of several hours [*Blanc and Richmond*, 1980] and is thought to be distinguishable from the prompt penetration field by the different time scale [e.g., *Scherliess and Fejer*, 1997]. The prompt penetration model by *Manoj and Maus* [2012] does not take into account the electric field effects from the disturbance dynamo. Therefore, in order to investigate contribution of the neutral wind disturbance dynamo effects we perform model simulation using the National Center for Atmospheric Research (NCAR) Thermosphere Ionosphere Electrodynamics General Circulation Model (TIE-GCM) model (version 1.95).

4.3.2. TIE-GCM Model Simulations

The TIE-GCM [*Roble et al*., 1988; *Richmond et al*., 1992] is a time-dependent, 3-D model that solves the fully coupled, nonlinear, hydrodynamic, thermodynamic, and continuity equations of the thermospheric neutral gas self-consistently with the ion continuity equations using a finite differencing scheme. The horizontal resolution is $5° \times 5°$ in geographic longitude and latitude, and the vertical resolution is 0.5 scale height in altitude. Here there employed a 20 min time step resolution. The magnetospheric input in the TIE-GCM consists of the specification of the high-latitude convection pattern and an auroral precipitation oval. The high-latitude potential was specified by *Heelis et al*.'s [1982] empirical model, which is parameterized by the geomagnetic *Kp* index. Further documentation of the model and its recent updates is available in [*Qian et al*., 2014, and references therein].

In the given study we are interested in the TIE-GCM simulations of the vertical plasma drift and neutral winds in equatorial and low-latitude ionosphere. Figure 6 presents the results of the TIE-GCM simulation run between 50°S and 50°N for different instants of time of 19 February 2014. On each graph neutral winds (vectors) are superimposed on a color contour plot of the vertical ion drift at the altitude of 500 km (the Swarm and TSX orbit). Movie S1 (available as supporting information) demonstrates the full series of these maps with 20 min time resolution for 19 February 2014. The presented results of the TIE-GCM simulation (Figure 6 and Movie S1) show the development of the storm-induced neutral winds circulation.

Usually, the vertical drifts are upward in the daytime sectors and downward in the nighttime sectors. Disturbance dynamo perturbations result from the global changes in the thermospheric winds that generate electric fields and currents through the ionospheric wind dynamo. The disturbance dynamo drives a downward plasma drift during the day and upward at night in opposition to the quiet time field. From ~06 UT (Movie S1) we can note the suppress of the maximal magnitude of the vertical drift at low latitudes for both daytime and nighttime sectors, owing to the disturbance dynamo effects. From ~09 UT along with further reduce of the daytime and nighttime vertical drift values, the formation of the enhanced upward vertical drift perturbations is observed close to the night-to-day border (the sunrise terminator). These perturbations in the form of the bulge-like structures, originated from the polar regions, moved equatorward from midlatitudes of both hemispheres. The vertical drift velocities inside both bulges increase with time up to 35–40 m/s. At 12–13 UT the two bulges arrive at the equator and merge into a single structure. These structures can be associated with traveling atmospheric disturbances. From 14 to 16 UT the single bulge with enhanced vertical drift values up to 45 m/s was observed between ±20° geographic latitudes and moved further westward with the dawn sector. So simulation results indicate that formation of the enhanced vertical drifts in the dawn sector was observed from 09 to 17 UT with maximal values of ~40–45 m/s during 12:00–15:30 UT, i.e., during our observations of very intensive ionospheric irregularities.

These enhanced upward vertical drift perturbations over middle and low latitudes co-locate with a rather narrow region where the thermospheric neutral winds with opposite directions converge. Figure 6i demonstrates more clearly the circulation of the thermospheric neutral winds at the altitude of 500 km for 13:20 UT. It is the modified version of Figure 6e with the enlarged latitude range of ±70° and reduced

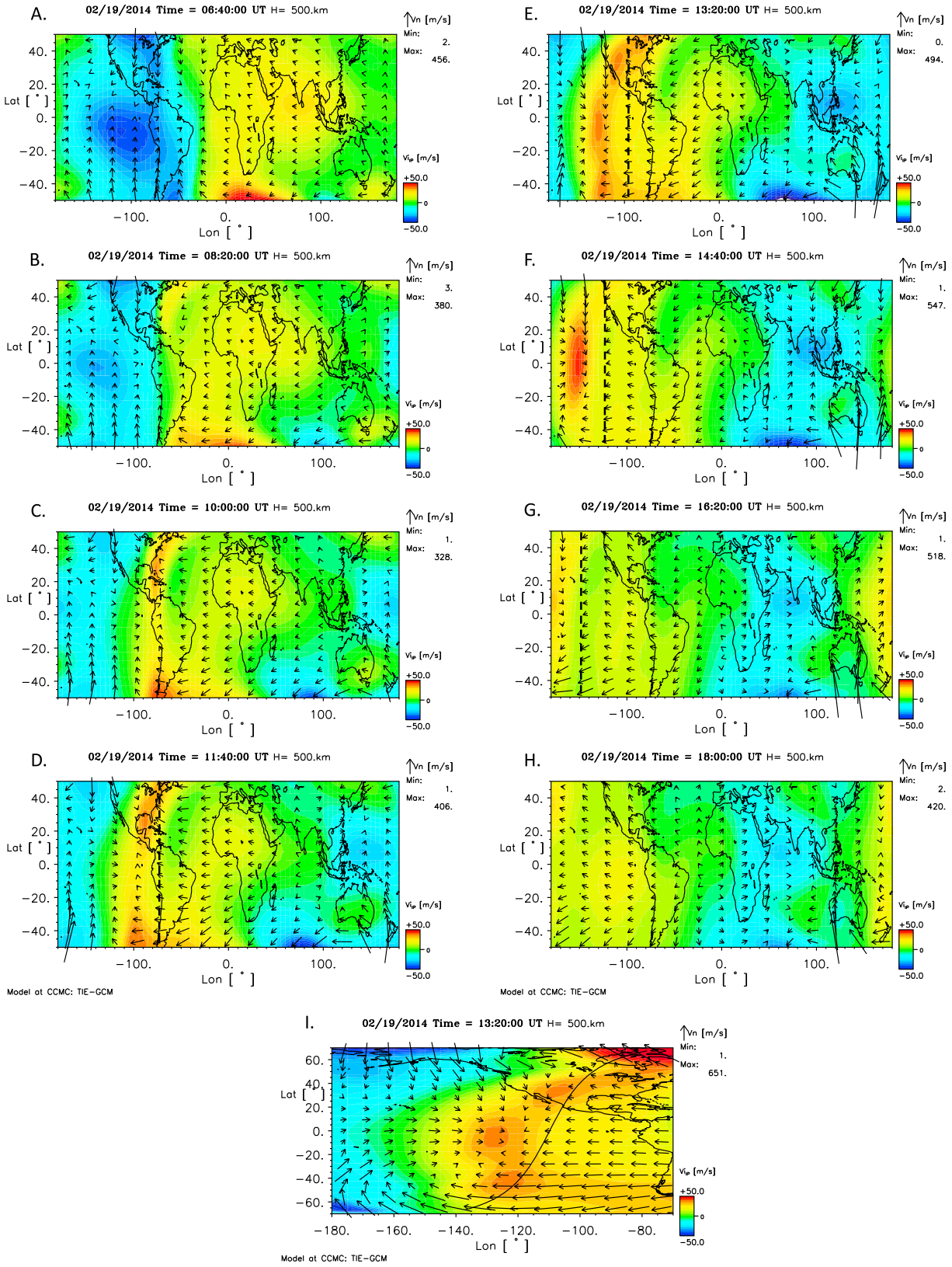

Figure 6. (a–h) Vertical ion drift (color) and thermospheric winds (vectors) at 500 km altitude modeled by the TIE-GCM for different instants of time on 19 February 2014. The black dashed line in Figures 6d–6g shows the SWB orbital track. (i) Same as above (case in Figure 6e) but enlarge to ±70° latitude plot for 13:20 UT. Black thin line indicates the sunrise terminator (ground level).

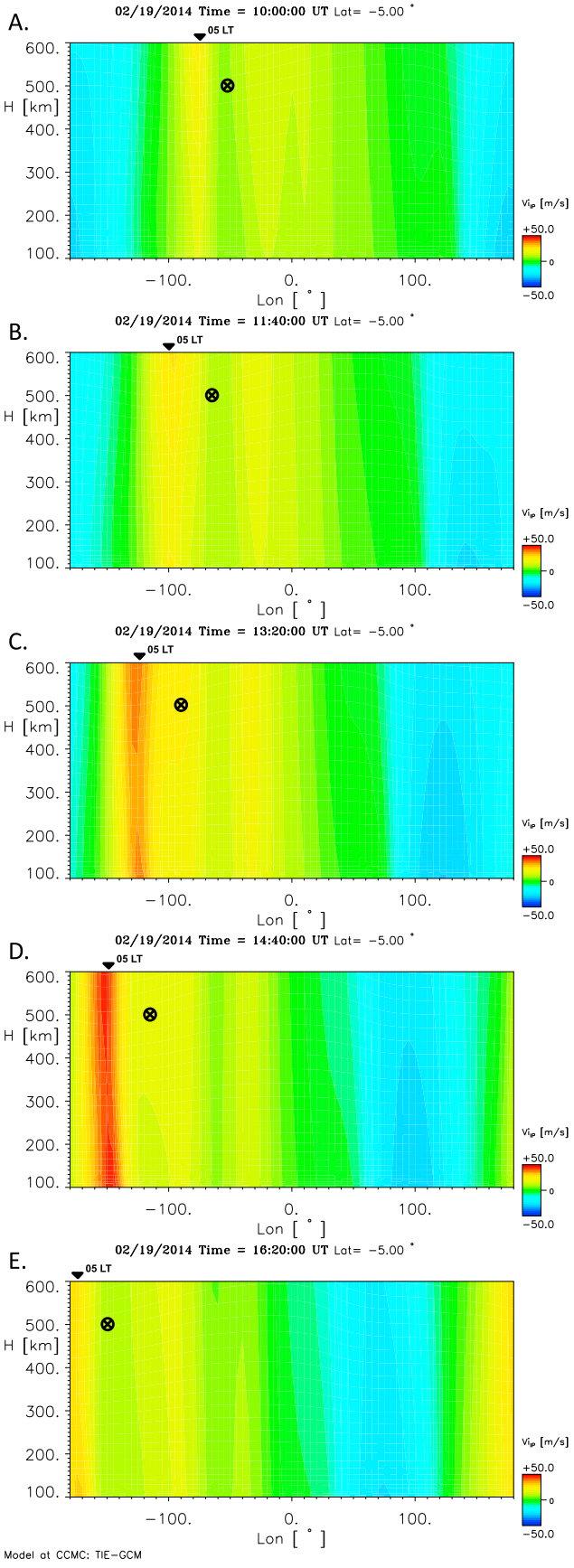

longitude range of 180°W–70°W. Model simulation results indicate the presence of the zonal winds of ~80–90 m/s over low latitudes, westward during the day and eastward during the night. The nighttime winds at the high latitudes are predominantly equatorward. Formation of the enhanced upward plasma drift perturbations is seen to be closely related to the disturbance dynamo neutral winds. The superimposed sunrise terminator demonstrates that zone with enhanced vertical drifts formed in the nonsunlit conditions close to dawn.

According to the TIE-GCM simulation results the maximal intensity of the enhanced upward vertical drift perturbations at the middle and low latitudes was registered from 09 to 17 UT on 19 February 2014 over the Pacific Ocean region, that is in a very good agreement with our results on the GPS-based detection of the ionospheric irregularities.

Figure 7 presents several examples of the TIE-GCM height-longitude variation of the vertical ion drift. These longitudinal slices (latitude 5°S) demonstrate the evidence of the early morning intensification of the vertical ion drifts at equatorial latitudes. Selected time intervals (similar to Figure 6) correspond to the time period when the SWB satellite appeared in the area. Maximal velocities of the upward drift were observed here at 13:20 and at 14:40 UT. The bright red vertical band, indicating the enhancement of the vertical plasma drift near 05 LT, is very similar to the TIE-GCM simulations and observation of the vertical drift corresponded to the evening time prereversal enhancement [e.g., *Rodrigues et al.*, 2012]. The SWB satellite (shown by crossed circle) was in advantage, nearby location from the zone of the peak vertical ion drifts favorable for the EPB generation.

Figure 7. (a–e) Height and longitude variation of the vertical ion drift for different instants of time, as simulated by the TIE-GCM. Black triangle at the top axis of each graph shows reference point of 05 LT. Location of the SWB satellite is marked by crossed circle.

Thus, the TIE-GCM results reveal the formation of the enhanced vertical drifts near the sunrise terminator for the geomagnetic storm conditions. Response of the equatorial vertical drifts to magnetic activity is strongly storm time dependent. The short-term disturbance dynamo, with time delay of 1–12 h between the high-latitude current enhancements and the equatorial velocity perturbations, drives upward equatorial drifts (eastward electric fields) at night with largest amplitudes near sunrise and small downward drifts during the day [*Scherliess and Fejer*, 1997].

Numerical simulation studies by *Fuller-Rowell et al*. [2002] predict the arrival of thermospheric disturbances at low latitude within only 2–3 h from the storm energy input at high latitudes. The dynamo action of the midlatitude wind surges drive an *F* region dynamo that can cause charge buildup at the terminators, producing electric fields that immediately leak to the equator. The model simulation results in [*Fuller-Rowell et al*., 2002] also indicate appearance of the enhanced eastward electric fields over low latitudes at early morning hours (05 LT) under the action of disturbance dynamo.

Numerical simulations of *Millward et al*. [2001] demonstrate importance of the lower thermospheric tidal forcing on the *F* region equatorial vertical ion drift. With the tidal forcing the authors report appearance of the dawn spikes ("postreversal enhancement") in the equatorial vertical drifts seen in the dawn sector (near 06 LT) even during quiet time conditions (June and December solstices of low solar activity).

According to these modeling results, the enhanced vertical drifts can occur at low and equatorial latitudes in the sunrise sector, driven by the thermospheric wind disturbance dynamo action. When the upward drift velocities are large enough, the necessary seeding mechanisms for the strong EPB generation always appear to be present [e.g., *Fejer et al*., 1999].

5. Conclusions

Using the data from GPS receivers on board the three Swarm and TSX satellites, we demonstrate the successful detection of the topside EPB in early morning hours (05–08 LT) during recovery phase of the 18–19 February geomagnetic storm. In February 2014, all of three Swarm satellites flew at 480–500 km of height, and in the same local sector. The morning time irregularities were observed for several consecutive orbits from ~11 UT to 16–17 UT on 19 February 2014 in the eastern Pacific low-latitude region, which suggests the following: (1) rather long duration (hours) of favorable conditions for EPB generation, (2) formation and evolution of EPB over wide longitude range of the Pacific Ocean, and (3) possible movement of the EPB region in the westward direction (with dawn). The GPS ROT/ROTI technique results demonstrate good agreement with the EPB observations in the concurrent in situ plasma density measurements at the three Swarm satellites.

Model simulation results demonstrate that EPB formation at early morning can be caused by the neutral wind disturbance dynamo action rather than the prompt penetration electric fields. The TIE-GCM results indicate the appearance of the zone with enhanced vertical plasma drift owing to the disturbance dynamo action in the predawn/dawn sector during 09–17 UT with maximal drift values of ~40–45 m/s during 12:00–15:30 UT. These results are in a strong agreement with our satellite observations. Also, model results explain why morning EPB were registered during several hours at several consequent satellite orbits over different longitudes of the Pacific Ocean, because zone with enhanced upward drifts moved westward with the sunrise terminator. Thereby, in this specific case the successful detection of the morning EPB was possible mainly due to a favorable orbit configuration of the Swarm constellation that moved in the morning LT sector during February 2014. Very fortunately, for this date and this time and this part of the Pacific Ocean the Swarm satellites passed nearby from the sunrise terminator and the zone with the enhanced upward drifts and favorable condition for the EPB generation and were able to trace the morning time EPB occurrence at several consequent satellite orbits.

In this case, the ground-based GPS and ionosonde stations could not provide any information for the region where satellites have detected the occurrence of the most intense EPB. Here satellite measurements, in particular LEO GPS measurements, can be much more informative to study the EPB occurrence. The obtained LEO ROT/ROTI results were confirmed by a very good consistency with the concurrent in situ plasma measurements. On the other hand, one of the undoubted advantage of LEO ROT/ROTI technique is the fact that while in situ measurements are straight-forward and probe the density point-by-point along a LEO position, this LEO-based GPS technique can track simultaneously up to 8–12 LOS with different GPS satellites

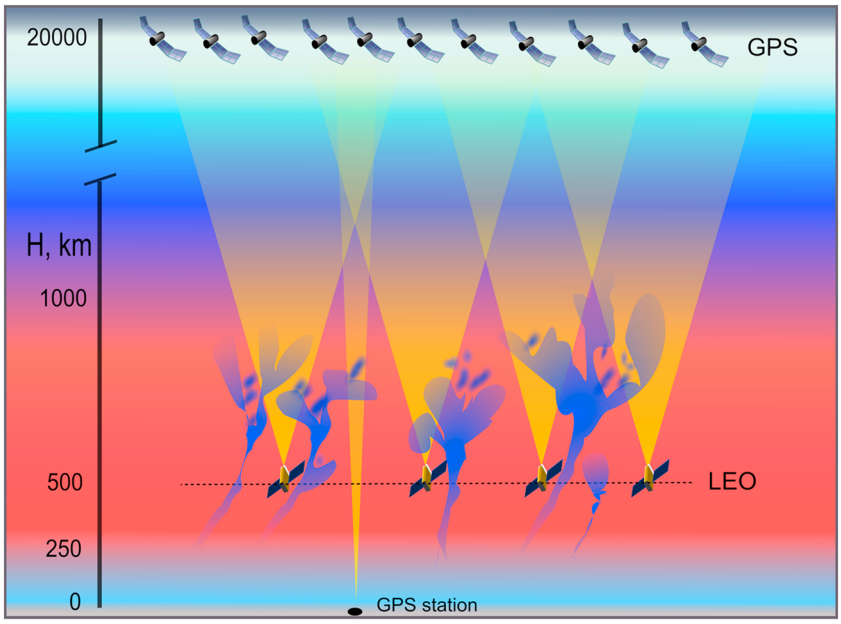

Figure 8. The sketch view of the GPS instrument configuration for the EPB detection: ground-based GPS station, LEO, and GPS constellation.

in great spatial volume above a LEO and is able to observe irregularities ahead/behind/aside LEO position and for much longer time than in situ cross section. Figure 8 presents a sketch of the discussed experiment. We note main features of the techniques: (1) a ground-based GPS station provides continuous 24 h measurements but it can detect the EPB only when they drift over this station; (2) LEO GPS can scan larger areas to detect the EPB occurrence, but limited in time; and (3) LEO GPS and LEO LP measurements can provide similar or even opposite results depending on the altitudinal extent of the EPB structures and LEO orbit altitude, when only one instrument is able to detect the EPB.

Our results demonstrate that the LEO ROT/ROTI technique has a great potential for detection the topside ionospheric irregularities occurrence on a global scale. For this specific case study the ionospheric irregularities were found over the Pacific Ocean, far from other ground-based facilities able to detect them. We emphasize that the main results were obtained with LEO GPS database provided by Swarm and TSX missions, as the Swarm LP observations were released only at February 2015 (more than a year after the mission launch). This means that the proposed technique can be effectively used for investigation of the topside irregularities even with the absence of LP instruments on board, e.g., for satellites TSX, GRACE, MetOP, SAC-C, and FORMOSAT-3/COSMIC.

References

Aarons, J., and B. Lin (1999), Development of high latitude phase fluctuations during the January 10, April 10–11, and May 15, 1997 magnetic storms, *J. Atmos. Sol. Terr. Phys.*, *61*(3–4), 309–327.

Aggson, T. L., H. Laakso, N. C. Maynard, and R. F. Pfaff (1996), In situ observations of bifurcation of equatorial ionospheric plasma depletions, *J. Geophys. Res.*, *101*(A3), 5125–5132, doi:10.1029/95JA03837.

Astafyeva, E., Y. Yasyukevich, A. Maksikov, and I. Zhivetiev (2014), Geomagnetic storms, super-storms, and their impacts on GPS-based navigation systems, *Space Weather*, *12*, 508–525, doi:10.1002/2014SW001072.

Basu, S., J. P. McClure, S. Basu, W. B. Hanson, and J. Aarons (1980), Coordinated study of equatorial scintillation and in situ and radar observations of nighttime *F* region irregularities, *J. Geophys. Res.*, *75*(A10), 5119–5130, doi:10.1029/JA085iA10p05119.

Basu, S., et al. (2001), Ionospheric effects of major magnetic storms during the International Space Weather Period of September and October 1999: GPS observations, VHF/UHF scintillations, and in situ density structures at middle and equatorial latitudes, *J. Geophys. Res.*, *106*(A12), 30,389–30,413, doi:10.1029/2001JA001116.

Blanc, M., and A. D. Richmond (1980), The ionospheric disturbance dynamo, *J. Geophys. Res.*, *85*(A4), 1669–1686, doi:10.1029/JA085iA04p01669.

Burke, W. J., R. C. Sagalyn, R. G. Rastogi, M. Ahmed, F. J. Rich, D. E. Donatelli, and P. J. L. Wildman (1979), Post-sunrise refilling of the low-latitude topside ionosphere, *J. Geophys. Res.*, *84*(A8), 4201–4206, doi:10.1029/JA084iA08p04201.

Burke, W. J., L. C. Gentile, C. Y. Huang, C. E. Valladares, and S. Y. Su (2004), Longitudinal variability of equatorial plasma bubbles observed by DMSP and ROCSAT-1, *J. Geophys. Res.*, *109*, A12301, doi:10.1029/2004JA010583.

Cherniak, I., A. Krankowski, and I. Zakharenkova (2014), Observation of the ionospheric irregularities over the Northern Hemisphere: Methodology and service, *Radio Sci.*, *49*, 653–662, doi:10.1002/2014RS005433.

Acknowledgments

This work is supported by the European Research Council under the European Union's Seventh Framework Program/ERC grant agreement 307998. We acknowledge the use of NASA/GSFC's Space Physics Data Facility's OMNIWeb service for the data of the interplanetary and geophysical parameters. We thank ESA for the SWARM data (http://earth.esa.int/swarm) and NGDC NOAA for access to DMSP data (satdat.ngdc.noaa.gov/dmsp/). We are grateful to ISDC GFZ Potsdam for providing TerraSAR-X data (isdc.gfz-potsdam.de) and IGS for GPS products (ftp://cddis.gsfc.nasa.gov). We acknowledge the use of the real-time model of the ionospheric electric fields (http://geomag.org/models/PPEFM/RealtimeEF.html). Simulation results have been provided by the Community Coordinated Modeling Center at Goddard Space Flight Center through their public Runs on Request system (http://ccmc.gsfc.nasa.gov). The CCMC is a multiagency partnership between NASA, AFMC, AFOSR, AFRL, AFWA, NOAA, NSF, and ONR. The TIE-GCM model was developed at the U.S. National Center for Atmospheric Research by Raymond G. Roble and collaborators. The TIE-GCM simulation outputs used in this study are available at the CCMC website. We thank B.W. Reinisch, UML, for providing the digisonde data of DIDBase. GPS RINEX data for Jicamarca station were provided by the LISN (lisn.igp.gob.pe). LISN is a project led by Boston College in collaboration with the Geophysical Institute of Peru and other institutions that provide information in benefit of the scientific community. This is IPGP contribution number 3677.

Alan Rodger thanks the reviewers for their assistance in evaluating the paper.

de La Beaujardière, O., et al. (2009), C/NOFS observations of deep plasma depletions at dawn, *Geophys. Res. Lett.*, *36*, L00C06, doi:10.1029/2009GL038884.
Demyanov, V. V., Y. V. Yasukevich, A. B. Ishin, and E. I. Astafyeva (2012), Effects of ionosphere super-bubble on GPS performance depending on the bubble orientation relative to geomagnetic field, *GPS Solutions*, *16*(2), 181–189, doi:10.1007/s10291-011-0217-9.
Farley, D. T., B. B. Balsley, R. F. Woodman, and J. P. Mc-Clure (1970), Equatorial spread-F: Implications of VHF radar observations, *J. Geophys. Res.*, *75*(34), 7199–7216, doi:10.1029/JA075i034p07199.
Fejer, B. G. (1991), Low latitude electrodynamic plasma drifts: A review, *J. Atmos. Terr. Phys.*, *53*(8), 677.
Fejer, B. G. (1997), The electrodynamics of the low-latitude ionosphere: Recent results and future challenges, *J. Atmos. Sol. Terr. Phys.*, *59*(13), 1465–1482.
Fejer, B. G., and M. C. Kelley (1980), Ionospheric irregularities, *Rev. Geophys. Space Phys.*, *18*(2), 401–454.
Fejer, B. G., L. Scherliess, and E. R. de Paula (1999), Effects of the vertical plasma drift velocity on the generation and evolution of equatorial spread F, *J. Geophys. Res.*, *104*(A9), 19,859–19,869, doi:10.1029/1999JA900271.
Fuller-Rowell, T. J., G. H. Millward, A. D. Richmond, and M. V. Codrescu (2002), Storm-time changes in the upper atmosphere at low latitudes, *J. Atmos. Sol. Terr. Phys.*, *64*(12–14), 1383–1391, doi:10.1016/S1364-6826(02)00101-3.
Heelis, R. A., J. K. Lowell, and R. W. Spiro (1982), A model of the high-latitude ionospheric convection pattern, *J. Geophys. Res.*, *87*(A8), 6339–6345, doi:10.1029/JA087iA08p06339.
Hofmann-Wellenhof, B. (2001), *Global Positioning System: Theory and Practice*, Springer, New York.
Huang, C. Y., W. J. Burke, J. S. Machuzak, L. C. Gentile, and P. J. Sultan (2002), Equatorial plasma bubbles observed by DMSP satellites during a full solar cycle: Toward a global climatology, *J. Geophys. Res.*, *107*(A12), 1434, doi:10.1029/2002JA009452.
Huang, C.-S., O. de La Beaujardière, P. A. Roddy, D. E. Hunton, J. Y. Liu, and S. P. Chen (2014), Occurrence probability and amplitude of equatorial ionospheric irregularities associated with plasma bubbles during low and moderate solar activities (2008–2012), *J. Geophys. Res. Space Physics*, *119*, 1186–1199, doi:10.1002/2013JA019212.
Hysell, D. L., and J. D. Burcham (1998), JULIA radar studies of equatorial spread F, *J. Geophys. Res.*, *103*(A12), 29,155–29,167, doi:10.1029/98JA02655.
Hysell, D. L., H. C. Aveiro, and J. L. Chau (2013), Ionospheric irregularities: Frontiers, *Geophys. Monogr. Ser.*, *201*, 217–240.
Jakowski, N., Y. Beniguel, G. De Franceschi, M. H. Pajares, K. S. Jacobsen, I. Stanislawska, L. Tomasik, R. Warnant, and G. Wautelet (2012), Monitoring, tracking and forecasting ionospheric perturbations using GNSS techniques, *J. Space Weather Space Clim.*, *2*, A22, doi:10.1051/swsc/2012022.
Jayachandran, B., N. Balan, P. B. Rao, J. H. Sastri, and G. J. Bailey (1993), HF Doppler and ionosonde observations on the onset conditions of equatorial spread F, *J. Geophys. Res.*, *98*(8), 13,741–13,750, doi:10.1029/93JA00302.
Kelley, M. C., J. J. Makela, O. Beaujardière, and J. Retterer (2011), Convective ionospheric storms: A review, *Rev. Geophys.*, *49*, RG2003, doi:10.1029/2010RG000340.
Kil, H., and R. A. Heelis (1998), Global distribution of density irregularities in the equatorial ionosphere, *J. Geophys. Res.*, *103*(A1), 407–417, doi:10.1029/97JA02698.
Livingston, R. C., C. L. Rino, J. P. McClure, and W. B. Hanson (1981), Spectral characteristics of medium-scale equatorial F region irregularities, *J. Geophys. Res.*, *86*(4), 2421–2428, doi:10.1029/JA086iA04p02421.
Lühr, H., C. Xiong, J. Park, and J. Rauberg (2014), Systematic study of intermediate-scale structures of equatorial plasma irregularities in the ionosphere based on CHAMP observations, *Front. Phys.*, *2*, 1–9, doi:10.3389/fphy.2014.00015.
Ma, G., and T. Maruyama (2006), A super bubble detected by dense GPS network at East Asian longitudes, *Geophys. Res. Lett.*, *33*, L21103, doi:10.1029/2006GL027512.
Manoj, C., and S. Maus (2012), A real-time forecast service for the ionospheric equatorial zonal electric field, *Space Weather*, *10*, S09002, doi:10.1029/2012SW000825.
Millward, G. H., I. C. F. Müller-Wodarg, A. D. Aylward, T. J. Fuller-Rowell, A. D. Richmond, and R. J. Moffett (2001), An investigation into the influence of tidal forcing on f region equatorial vertical ion drift using a Global Ionosphere-Thermosphere Model with Coupled Electrodynamics, *J. Geophys. Res.*, *106*(A11), 24,733–24,744, doi:10.1029/2000JA000342.
Nishioka, M., A. Saito, and T. Tsugawa (2008), Occurrence characteristics of plasma bubble derived from global ground-based GPS receiver networks, *J. Geophys. Res.*, *113*, A05301, doi:10.1029/2007JA012605.
Ossakow, S. L. (1981), Spread F theories: A review, *J. Atmos. Terr. Phys.*, *43*, 437–452.
Ossakow, S. L., and P. K. Chaturvedi (1978), Morphological studies of rising equatorial spread F bubbles, *J. Geophys. Res.*, *83*(A5), 2085–2090, doi:10.1029/JA083iA05p02085.
Park, J., M. Noja, C. Stolle, and H. Lühr (2013), The ionospheric bubble index deduced from magnetic field and plasma observations onboard Swarm, *Earth Planets Space*, *65*(11), 1333–1344, doi:10.5047/eps.2013.08.005.
Pi, X., A. J. Mannucci, U. J. Lindqwister, and C. M. Ho (1997), Monitoring of global ionospheric irregularities using the worldwide GPS network, *Geophys. Res. Lett.*, *24*(18), 2283–2286, doi:10.1029/97GL02273.
Preliminary L1b plasma dataset (2015), Swarm document. [Available at http://swarm-wiki.spacecenter.dk/mediawiki-1.21.1/index.php/Preliminary_Level_1b_plasma_dataset, Accessed 25 August 2015.]
Qian, L., A. Burns, B. A. Emery, B. Foster, G. Lu, A. Maute, A. D. Richmond, R. G. Roble, S. C. Solomon and W. Wang (2014), The NCAR TIE-GCM: A community model of the coupled thermosphere/ionosphere system, in *Modeling the Ionosphere-Thermosphere System*, *Geophys. Monogr. Ser.*, vol. 201, edited by J. Huba, R. Schunk, and G. Khazanov, chap. 7, pp., 73–84, John Wiley, Chichester, U. K, doi:10.1002/9781118704417.
Reinisch, B. W. (1996), Modern ionosondes, in *Modern Ionospheric Science*, edited by H. Kohl, R. Rüster, and K. Schlegel, pp. 440–458, Eur. Geophys. Soc., Katlenburg-Lindau, Germany.
Reinisch, B. W., and I. A. Galkin (2011), Global Ionospheric Radio Observatory (GIRO), *Earth Planets Space*, *63*(4), 377–381.
Reinisch, B. W., J. L. Scali, and D. M. Haines (1998), Ionospheric drift measurements with ionosondes, *Ann. Geofis.*, *41*(5–6), 695–702.
Richmond, A. D., E. C. Ridley, and R. G. Roble (1992), A Thermosphere-Ionosphere General Circulation Model with Coupled Electrodynamics, *Geophys. Res. Lett.*, *19*(6), 601–604, doi:10.1029/92GL00401.
Roble, R. G., E. C. Ridley, A. D. Richmond, and R. E. Dickinson (1988), A Coupled Thermosphere/Ionosphere General Circulation Model, *Geophys. Res. Lett.*, *15*(12), 1325–1328, doi:10.1029/GL015i012p01325.
Rodrigues, F. S., M. C. Kelley, P. A. Roddy, D. E. Hunton, R. F. Pfaff, O. de La Beaujardière, and G. S. Bust (2009), C/NOFS observations of intermediate and transitional scale-size equatorial spread F irregularities, *Geophys. Res. Lett.*, *36*, L00C05, doi:10.1029/2009GL038905.
Rodrigues, F. S., G. Crowley, R. A. Heelis, A. Maute, and A. Reynolds (2012), On TIE-GCM simulation of the evening equatorial plasma vortex, *J. Geophys. Res.*, *117*, A05307, doi:10.1029/2011JA017369.
Scherliess, L., and B. G. Fejer (1997), Storm time dependence of equatorial disturbance dynamo zonal electric fields, *J. Geophys. Res.*, *102*(A11), 24,037–24,046, doi:10.1029/97JA02165.

Scherliess, L., and B. G. Fejer (1999), Radar and satellite global equatorial F region vertical drift model, *J. Geophys. Res.*, *104*(A4), 6829–6842, doi:10.1029/1999JA900025.

Sripathi, S., B. Kakad, and A. Bhattacharyya (2011), Study of equinoctial asymmetry in the equatorial spread F (ESF) irregularities over Indian region using multi-instrument observations in the descending phase of solar cycle 23, *J. Geophys. Res.*, *116*, A11302, doi:10.1029/2011JA016625.

Stolle, C., H. Lühr, M. Rother, and G. Balasis (2006), Magnetic signatures of equatorial spread F as observed by the CHAMP satellite, *J. Geophys. Res.*, *111*, A02304, doi:10.1029/2005JA011184.

Tsunoda, R. T., R. C. Livingston, J. P. McClure, and W. B. Hanson (1982), Equatorial plasma bubbles: Vertically elongated wedges from the bottomside F layer, *J. Geophys. Res.*, *87*(A11), 9171–9180, doi:10.1029/JA087iA11p09171.

Woodman, R. F., and C. La Hoz (1976), Radar observations of F region equatorial irregularities, *J. Geophys. Res.*, *81*(31), 5447–5466, doi:10.1029/JA081i031p05447.

Xiong, C., J. Park, H. Lühr, C. Stolle, and S. Y. Ma (2010), Comparing plasma bubble occurrence rates at CHAMP and GRACE altitudes during high and low solar activity, *Ann. Geophys.*, *28*(9), 1647–1658, doi:10.5194/angeo-28-1647-2010.

Yeh, H. C., S.-Y. Su, and R. A. Heelis (2001), Storm time plasma irregularities in the pre-dawn hours observed by the low-latitude ROCSAT-1 satellite at 600 Km, *Geophys. Res. Lett.*, *28*(4), 685–688, doi:10.1029/2000GL012183.

Zakharenkova, I., and E. Astafyeva (2015), Topside ionospheric irregularities as seen from multisatellite observations, *J. Geophys. Res. Space Physics*, *120*, 807–824, doi:10.1002/2014JA020330.